

MATERIALS SCIENCE

Aluminum formate, Al(HCOO)₃: An earth-abundant, scalable, and highly selective material for CO₂ capture

Hayden A. Evans^{1†}, Dinesh Mullangi^{2†}, Zeyu Deng^{2†}, Yuxiang Wang^{3†}, Shing Bo Peh^{3†}, Fengxia Wei⁴, John Wang², Craig M. Brown^{1,5}, Dan Zhao^{3*}, Pieremanuele Canepa^{2,3*}, Anthony K. Cheetham^{2,6*}

A combination of gas adsorption and gas breakthrough measurements show that the metal-organic framework, Al(HCOO)₃ (ALF), which can be made inexpensively from commodity chemicals, exhibits excellent CO₂ adsorption capacities and outstanding CO₂/N₂ selectivity that enable it to remove CO₂ from dried CO₂-containing gas streams at elevated temperatures (323 kelvin). Notably, ALF is scalable, readily pelletized, stable to SO₂ and NO, and simple to regenerate. Density functional theory calculations and in situ neutron diffraction studies reveal that the preferential adsorption of CO₂ is a size-selective separation that depends on the subtle difference between the kinetic diameters of CO₂ and N₂. The findings are supported by additional measurements, including Fourier transform infrared spectroscopy, thermogravimetric analysis, and variable temperature powder and single-crystal x-ray diffraction.

INTRODUCTION

Efficient CO₂ capture and storage technologies can reduce the environmental impact of fossil fuel use. Conventional chemical sorbents based on aqueous amine solutions have a considerable capacity for postcombustion CO₂ capture but have the disadvantages of thermal degradation, corrosion, oxidative reactions, and usually energy-intensive regeneration processes (1). Porous solid sorbents that capture CO₂ through physisorption require less energy for regeneration and have great potential for cost-effective CO₂ capture (2). However, traditional solid sorbents, such as zeolites and porous carbon-based materials, also have considerable limitations. In particular, aluminosilicate zeolites have inadequate CO₂ uptake capacity in humid gas streams, and porous polymer and carbonaceous materials have low adsorption capacities and poor CO₂/N₂ selectivities (3).

Metal-organic frameworks (MOFs), with their high surface areas, tunable pore sizes, surface functionality, and structural diversity, offer several advantages as the next-generation solid adsorbent materials for CO₂ capture (4, 5) but have limitations of their own. These usually include sensitivity to humidity, poor mechanical properties, and, for many high-performing MOF materials, complex ligand precursors that may be too costly for large-scale applications. In the present work, we address the cost and scalability issues by exploring the adsorption properties of one of the simplest of all MOFs, aluminum formate, Al(HCOO)₃ (ALF). ALF is a mechanically robust material that can be made from the inexpensive and

widely available starting reagents, aluminum hydroxide and formic acid. It exhibits excellent CO₂ adsorption properties and CO₂/N₂ selectivities for dried CO₂-containing gas streams.

Postcombustion flue gases typically contain CO₂ (8 to 16%), O₂ (3 to 4%), and H₂O (5 to 7%), with N₂ comprising the balance. Several MOFs have shown substantial gravimetric CO₂ uptake capacities for dried flue gas streams. For example, the widely studied Mg-MOF-74, based on the ligand 2,5-dihydroxyterephthalate (dhtp), has a leading gravimetric capacity of 8.04 mmol/g (1 bar/298 K) (4). There are also MOFs with open metal sites or Lewis base sites or both, micropores (4 Å to 6 Å), and excess polar functionalities—such as hydroxyl, amino, pyridyl, and thiol—that have shown considerable CO₂ adsorption capacities (4, 5). These materials would require a drying step before CO₂ capture to be practical, adding extra cost to the overall process. Other MOFs, however, perform quite well in wet flue gas streams, drawing attention to the importance of understanding the role of water with CO₂ adsorption in each material class (6). For example, the SIFSIX family of materials show impressive performance under realistic flue gas conditions (7–9), but they contain expensive constituents. The state-of-the-art MOF material for postcombustion CO₂ capture is CALF-20, which shows excellent CO₂/N₂ selectivity and good stability in wet gas streams, among other qualities (10–12). However, even CALF-20 faces cost and scalability challenges because its chemical composition, Zn₂(1,2,4-triazole)₂(oxalate), requires the use of a triazolite and a relatively expensive zinc precursor. Thus, it remains extremely challenging to find MOFs that can capture CO₂ from combustion point sources in a cost-effective and scalable manner (13). An alternative approach, which we explore in the present work, is to reduce the cost of the MOFs to the point where a drying step, before CO₂ capture, becomes a viable option.

RESULTS AND DISCUSSION

The use of the metal(III) formates, M^{III}(HCOO)₃, where M = Al, Fe, Ga, In, and Mn (14), for small molecular separations and gas capture applications has not been reported previously. The parent structure of these compounds is of the ReO₃ type (15), but the M^{III}

¹Center for Neutron Research, National Institute of Standards and Technology, Gaithersburg, MD 20899, USA. ²Department of Materials Science and Engineering, National University of Singapore, 9 Engineering Drive 1, Singapore 117575, Singapore.

³Department of Chemical and Biomolecular Engineering, National University of Singapore, 4 Engineering Drive 4, Singapore 117585, Singapore. ⁴Institute of Materials Research and Engineering, Agency for Science Technology and Research, 2 Fusionopolis Way, Innovis, Singapore 138634, Singapore. ⁵Department of Chemical and Biomolecular Engineering, University of Delaware, Newark, DE 19716, USA.

⁶Materials Research Laboratory, University of California, Santa Barbara, Santa Barbara, CA 93106, USA.

*Corresponding author. Email: chezhao@nus.edu.sg (D.Z.); pcanepa@nus.edu.sg (P.C.); akc30@cam.ac.uk (A.K.C.)

†These authors contributed equally to this work.

formate compounds have only hitherto been reported as their CO₂/water adducts, e.g., Al(HCOO)₃·(CO₂)_{3/4}·(H₂O)_{1/4}·(HCOOH)_{1/4} with CO₂, water, and/or formic acid filling the perovskite *A*-site cavities. This material, referred to here as the as-made Al(HCOO)₃ (14), was prepared by reacting aluminum hydroxide with formic acid (see Materials and Methods). We activated (removed the guest species) the as-made Al(HCOO)₃ material either in vacuum between 373 and 403 K or by heating to ≈473 K in air at ambient pressure. The activated Al(HCOO)₃, referred to here as ALF, retained its structure after exposure to air, solvents, and corrosive media and was thermally stable up to ≈523 K in air (figs. S8 to S10 and S14).

The crystal structure of ALF (Fig. 1A) was obtained from Rietveld refinement with neutron powder diffraction (NPD) data; the fractional coordinates agree with the structure obtained by single-crystal x-ray diffraction (table S1) and energy minimization using density functional theory (DFT) calculations (tables S2 and S3). The crystal structure of ALF has two types of cavities, which we refer to as the small cavities (SCs) and the large cavities (LCs). There are three times as many SCs as LCs, and the SC and LC pore volumes at 300 K are 43(3) and 79(9) Å³, respectively (obtained using PLATON) (16). For the SCs, 4 of the 12 formate ligands point their hydrogens inward (Fig. 1E); and for the LCs, all 12 of the formate ligands point their hydrogens outward (Fig. 1F).

The inward-pointing formate hydrogens facilitated a favorable hand-in-glove relation between CO₂ and the SCs. Furthermore, the crystal structure contained two types of interpenetrating channels (Fig. 1B). One channel comprised only SCs (gray squares), and the other comprised alternating SCs and LCs (purple circles). As discussed below, a favorable window size along the SC/LC channels relative to the SC/SC channels [4.561(7) and 4.103(19) Å, respectively (figs. S6 and S7)] favored CO₂ adsorption in the SC/LC channels. The

Brunauer-Emmett-Teller surface area of ALF was estimated to be 588 ± 8 m² g⁻¹ (error is 1σ; fig. S23).

As shown in Fig. 2 (A and B), despite the microporosity of ALF, it did not adsorb N₂ at 298 K and at all practically useful temperatures (see fig. S20) but readily adsorbed CO₂ at and above 273 K. The low-pressure CO₂ uptake was substantial and persisted to 323 K with noticeable desorption hysteresis loops, suggesting appreciable diffusion barriers for CO₂ in the SC/SC channels of ALF (see fig. S19). ALF's affinity for water was much reduced compared with other leading MOFs that are known to be hydrophilic, such as MOF-74-Ni and UiO-66-(OH)₂ (Fig. 2C), but it is not negligible, as discussed below.

Although most experimental screening efforts concentrate on CO₂ uptake at near-ambient temperature, 298 K, the practical implementation favors a slightly higher operating temperature due to other pretreatment units for the postcombustion flue gas. ALF performed well under these conditions, as shown by our dynamic column breakthrough experiments at 323 K using a simulated feed (15/85 mixture of CO₂ and N₂). The CO₂ concentration front was substantially delayed compared to that of N₂ because of selective adsorption by ALF packed within the column (Fig. 2D; experimental details in Materials and Methods). The calculated capacity of CO₂ coadsorption was 0.8 mmol g⁻¹, whereas the N₂ counterpart was barely detectable (<0.1 mmol g⁻¹). Furthermore, these characteristics are largely retained in the presence of SO₂ and NO (fig. S27), suggesting excellent stability of ALF against corrosive gases. In terms of the system's cyclability, the guest-free MOF could be regenerated by heating to 353 K under a CO₂ atmosphere and was stable over more than 100 cycles (Fig. 2E and fig. S15, top).

We have also explored the performance of ALF under wet flue gas conditions. Experiments in which columns were presaturated by moisture [relative humidity (RH) = 80.5%] maintained 70% of

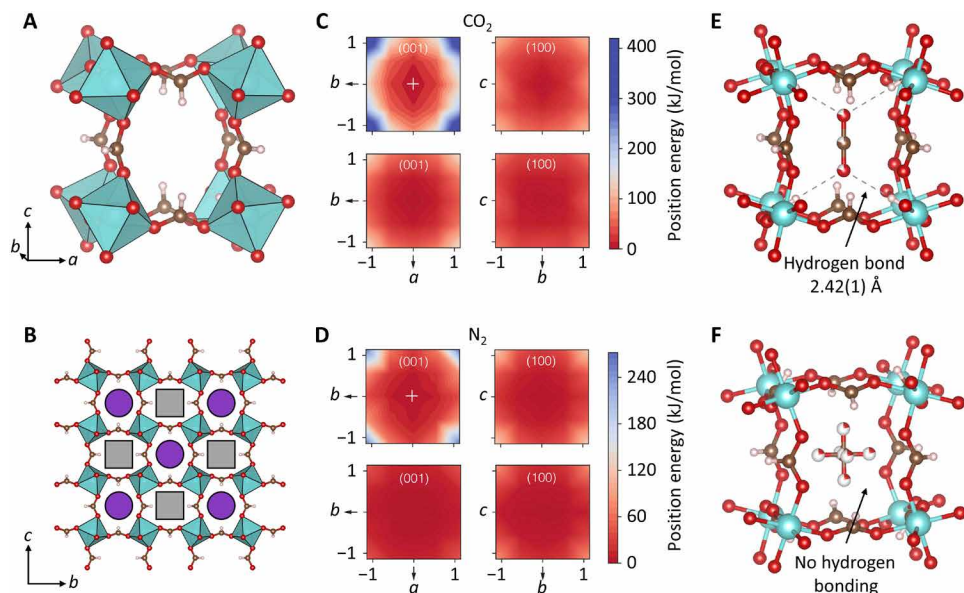


Fig. 1. Experimental and theoretical results on the structure of ALF with and without CO₂. (A) The structure of ALF at 300 K determined from neutron diffraction. Space group = *Im* $\bar{3}$; *a* = 11.3905(1); *V* = 1477.85(5). (B) Structure of ALF illustrating the two types of interpenetrating LC-SC-LC (purple circles) and SC-SC-SC (gray squares) channels within ALF. (C and D) Position energy of CO₂ and N₂ as the molecules are translated in the small cavity (SC; upper boxes) and large cavity (LC; lower boxes) of ALF. In (C) and (D), positive energies (blue areas in the color maps) represent energetically unfavorable positions, and white crosses serve as guides for the eye. The absolute values of the position energies are different in (C) and (D). (E) SC, illustrating hydrogen bonding with formate ligands and CO₂. Error value is 1σ. (F) LC, illustrating lack of hydrogen bonding.

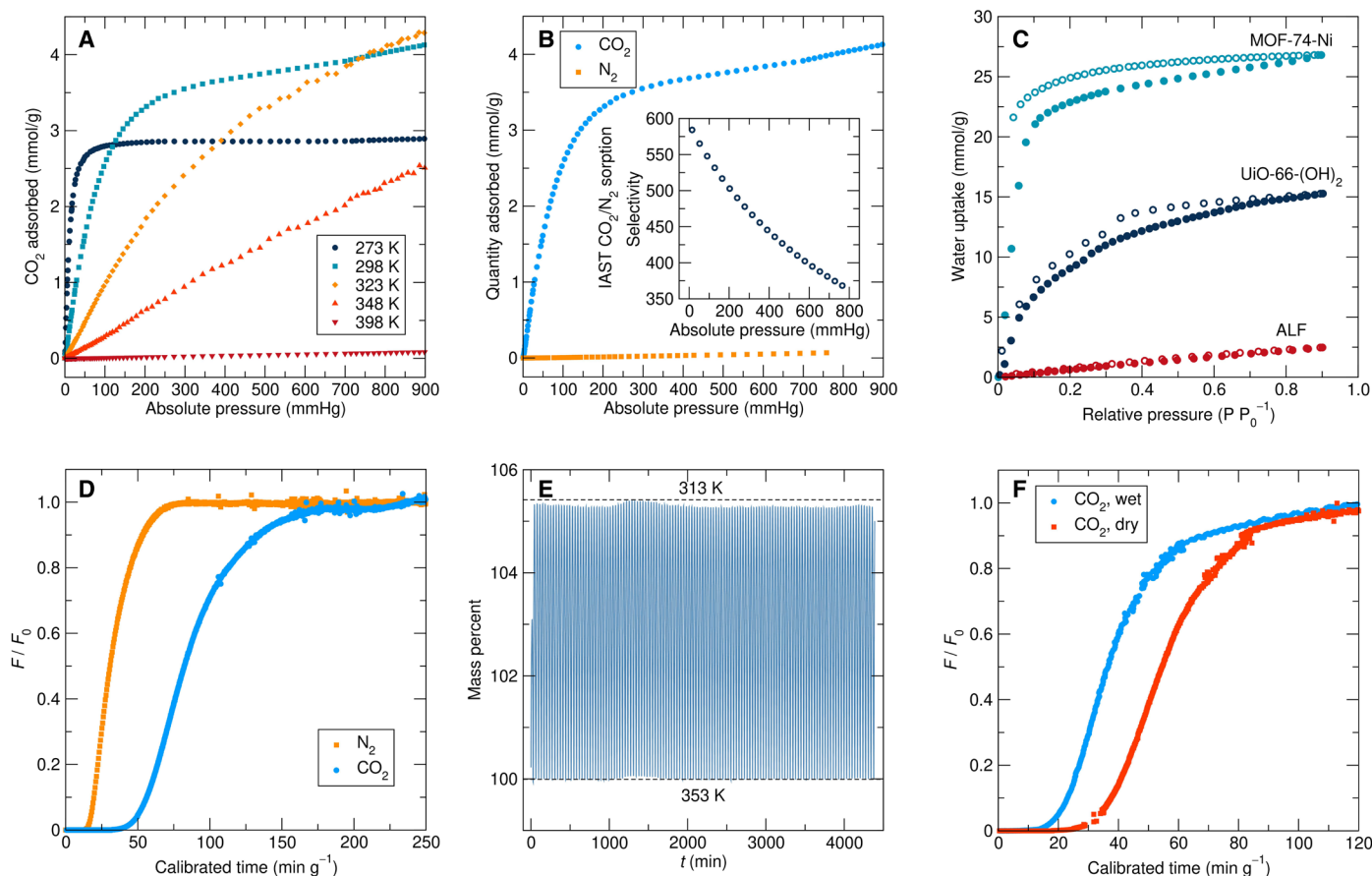


Fig. 2. Isotherm and breakthrough adsorption data. (A) CO_2 adsorption isotherms at various temperatures. (B) Comparison of the CO_2 and N_2 adsorption isotherms at 298 K. The inset shows the CO_2/N_2 sorption selectivity based on ideal adsorbed solution theory (IAST; defined in Materials and Methods) for a 15/85 mixture of CO_2/N_2 at 298 K (323 K in fig. S28). (C) Comparison of the H_2O vapor sorption isotherms of ALF, MOF-74-Ni, and UiO-66-(OH) $_2$ at 298 K. (D) Breakthrough curves (uncalibrated) of a 15/85 CO_2/N_2 mixed gas through an ALF-packed column at 323 K. The CO_2 uptake and CO_2/N_2 selectivity from these curves were 0.80(1) mmol/g and 75(21), respectively. (E) In situ thermogravimetric analysis (TGA) cycling studies on ALF under dry CO_2 atmosphere. This graph shows 130 cycles where degassing occurs at 353 K and CO_2 adsorption takes place on cooling to 313 K. Each cycle was approximately 30 min. (F) Comparison of the CO_2 breakthrough curves through ALF packed column at 323 K under dry and wet conditions. For wet conditions, the column was presaturated by moisture before introducing wet CO_2/N_2 mixed gas. The curves are calibrated after point-by-point (PBP) correction (see Materials and Methods). Virial fits for the CO_2 isotherms collected can be found in fig. S22. Langmuir fits and pore size distribution can be found in figs. S24 and S25, respectively.

their CO_2 dynamic capacity (fig. S38), suggesting that CO_2 could outcompete H_2O guests for sites within ALF. Usually, this level of CO_2 preference versus H_2O in MOFs requires chemisorption sites like alkyl amine moieties (table S7). While these results suggest that ALF exhibits promising physisorptive CO_2 capture characteristics under wet postcombustion flue gas conditions, further experiments have shown that the system is, nevertheless, sensitive to moisture under certain circumstances. As can be seen from dynamic vapor sorption (DVS) experiments performed on ALF at 303, 313, and 323 K with N_2 or CO_2 carrier gases (fig. S36), at 303 K, ALF could withstand water concentrations up to 90% saturation without degradation with CO_2 carrier gas. However, at 313 and 323 K, there was $\approx 2\%$ mass loss with CO_2 carrier gas. Under N_2 , degradation occurred at all tested temperatures. A noticeable difference between the N_2 and CO_2 experiments is that the degradation of ALF is approximately three- to fourfold less when CO_2 is used as the carrier gas. This indicates that the presence of CO_2 imparts a partial defense against water-induced material degradation. These DVS experiments indicate that, although ALF likely cannot be used to directly treat

postcombustion flue gas saturated with moisture, it shows promise when coupled with a suitable upstream drying technology. Drying to ALF's stability envelope ($\approx 25\%$ RH at 323 K) may be realized by relatively cheap and facile approaches such as cooling and condensation (17), contrasting the necessity for deep drying to as low as <100 parts per million [dew point, -40°C (233 K)] to circumvent binding site poisoning for highly hygroscopic sorbents. Furthermore, ALF's resilience to humidity near room temperature facilitates easy handling and storage without inert atmosphere or other cumbersome precautions if used on an industrial scale.

To probe why ALF adsorbs CO_2 so effectively, DFT calculations were performed to map the energy landscapes of both CO_2 and N_2 inside the two cavities (SCs and LCs) of ALF (Fig. 1, C and D) (18). The DFT adsorption energies of CO_2 , N_2 , and H_2O were computed within the generalized gradient approximation (GGA), where the exchange-correlation functional was approximated as proposed by Perdew-Burke-Ernzerhof (19). van der Waals forces were accounted for with the DFT-D3 correction scheme proposed by Grimme *et al.* (20). Details of the simulations are provided in Materials and Methods.

From the adsorption energies of CO₂ and N₂ in ALF presented in Table 1, we drew two main conclusions. First, the adsorption energy was greater for CO₂ than N₂ in both cavities. Second, CO₂ was preferentially adsorbed in the SC of ALF, whereas N₂ showed no preference for either cavity. These results are further emphasized in Fig. 1 (C and D), which show that, in the SCs, CO₂ preferred to orient along the *c* axis toward the inward-pointing hydrogens, whereas the energy landscape was flat in the LC with a slight preference for the center of the cavity. For N₂, the energy landscape was flat for both the SC and LC, with a slight preference to the center of the cavity. DFT calculations (Table 1) also show that H₂O (−51.3 kJ/mol) adsorption was slightly more favorable than CO₂ (−48.4 kJ/mol) in the SC, whereas the CO₂ adsorption was strongly preferred in the LC. The similarity in adsorption energies of CO₂ and H₂O implies less adverse competition for binding sites between CO₂ and H₂O compared to other hydrophilic materials (−60 kJ/mol < Δ*H* < −100 kJ/mol) where H₂O binding energies/enthalpies are substantially higher. This is initially suggested by the substantial retention of dynamic capacity in the wet gas breakthrough experiments and modeled mixture adsorption profiles (Fig. 2F and fig. S35). Further experiments, however, as described above, showed gradual degradation of the ALF at high moisture concentrations (fig. S36). For the flue gas application, therefore, we again conclude that a drying step will be required before CO₂ capture in any commercial implementation.

Figure 3A illustrates the Rietveld refinement fits of ALF with and without CO₂. Nondeuterated samples of ALF were used for all NPD experiments, which led to a sloping background because of the incoherent scattering of hydrogen. Figure 3 (A and B) shows selected results from NPD experiments on CO₂ adsorbed into ALF performed at 320 K with various partial pressures of CO₂. This temperature was chosen on the basis of the isotherms of pure CO₂ (fig. S19), which indicated that, relative to 300 K, CO₂ adsorption at 320 K had improved kinetics. It can be seen in Fig. 3B (top) that, when ALF was exposed to increasing pressures of CO₂, the lattice parameter of ALF gradually contracted. We note that the increased CO₂ adsorption seen between 273 and 323 K (Fig. 2A) is likely due to the expansion of the ALF unit cell over this temperature range and the increased dynamics of the formate groups.

Figure 3B (bottom) shows the increasing crystallographic occupancies of CO₂ in both the SCs and LCs as the pressure increases. Note that the occupancy of CO₂ in the SCs was consistently higher than that in the LCs (Fig. 3B), which was consistent with the adsorption energies from DFT (Table 1). At the highest CO₂ loading in Fig. 3B, the occupancy of the SC was ≈90%, whereas that of the LC was ≈50%, giving an approximate overall composition of Al(HCOO)₃(CO₂)_{0.78} (recalling that there are three times as many

SCs than LCs). This occupancy corresponds to a CO₂ loading of ≈4.8 mmol/g. The CO₂ loading into ALF under these conditions is slightly increased when compared with the initial level of CO₂ present in the as-made Al(HCOO)₃, as the latter only accommodated CO₂ in the SCs (14).

The comparison between the SCs hand-in-glove hydrogen-bonding association with CO₂ relative to the LCs is shown in Fig. 1 (E and F). In our model, CO₂ moved through the LC/SC channel more efficiently because of the larger window size along the LC/SC channel. Thus, the distinctive feature of ALF is that these windows appeared to be just large enough to permit the facile adsorption of CO₂ but not large enough to permit the adsorption of N₂, noting that the kinetic diameter of CO₂ (≈3.3 Å) is slightly smaller than that of N₂ (≈3.64 Å) (21). This subtle size difference enabled ALF to achieve the observed kinetic separation of CO₂ and

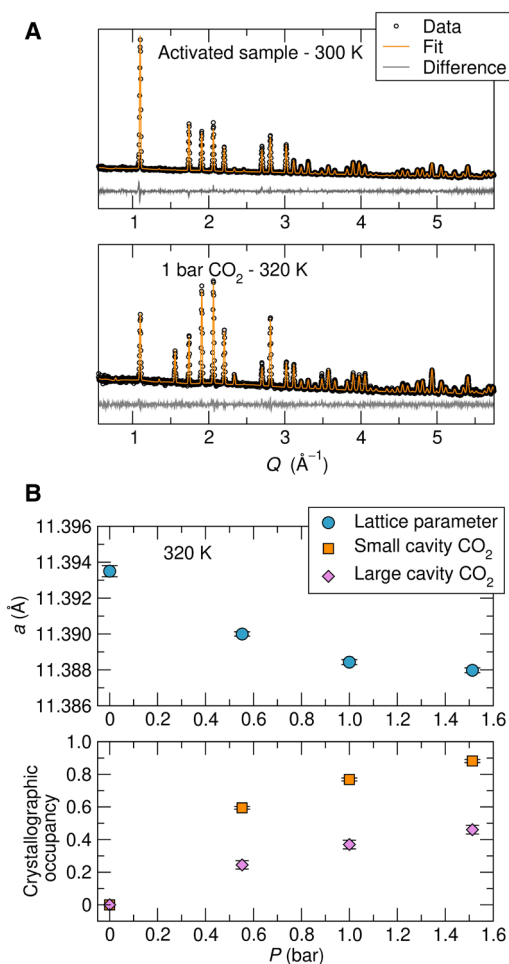


Fig. 3. Neutron diffraction results from experiments on ALF (National Institute of Standards and Technology Center for Neutron Research, BT1, $\lambda = 2.079 \text{ \AA}$). (A) Top: Rietveld refinement fit of activated ALF at 300 K; $a = 11.39051(12)$, $R_{wp} = 2.74\%$, $R_p = 2.19\%$. Bottom: Rietveld refinement fit of ALF exposed to 1 bar of CO₂ at 320 K; $R_{wp} = 3.35\%$, $R_p = 3.43\%$. The scan time for the activated sample data was twice that of the CO₂ exposed data. Change in lattice parameter of activated sample versus temperature is shown in fig. S1. Refinements of other datasets are shown in figs. S2 to S4. (B) Top: Lattice parameters obtained from Rietveld refinements as a function of CO₂ dosing pressure for ALF at 320 K. Bottom: CO₂ crystallographic occupancies obtained from Rietveld refinements as a function of the CO₂ dosing pressure for ALF at 320 K. Error bars in graphs denote 1 σ .

Table 1. Adsorption energies from first-principles calculations (in kilojoules per mole) and experimental isosteric enthalpy of adsorption. The isosteric enthalpy of adsorption is measured at low molecular loadings (≈1 mmol/g) from the CO₂ gas adsorption isotherms (fig. S21) and is in good agreement with the DFT results for the SC.

Molecule	Small cavity (kJ/mol)	Large cavity (kJ/mol)	Isosteric enthalpy of adsorption (kJ/mol)
CO ₂	−48.4	−36.2	−47.7
N ₂	−28.4	−28.6	−
H ₂ O	−51.3	−28.8	−

N₂. While most MOFs that show good selectivity for CO₂ over N₂ do so by using nitrogen-containing linkers to enhance the chemical affinity of the cavities for CO₂, we note that the SIFSIX family, like ALF, uses size selectivity (7–9). We also note that, while hand-in-glove CO₂ binding situations are unusual in MOFs, the siting of CO₂ in the SIFSIX family of compounds is also similarly favorable.

ALF has some other attractive features that set it apart from other MOF sorbents. It is readily prepared on a kilogram scale in the laboratory (fig. S29) with formic acid acting as both a reactant and a solvent, so no additional solvent is required. We estimate that the material cost for obtaining ALF on the metric ton scale from two commodity chemicals, aluminum hydroxide and formic acid, is only ≈\$1000 per metric ton, making it substantially cheaper than any of the other MOF alternatives, including CALF-20. We propose that this cost reduction could enable the inclusion of a drying step in the flue gas treatment process costing as low as \$2 per metric ton CO₂ captured in certain embodiments (22). Furthermore, ALF has excellent mechanical properties (table S9) that are superior to those of most MOFs (23), wherein it can be pelletized and even ball-milled while retaining performance (fig. S30). ALF also benefits from good volumetric performance on account of its relatively high density (table S7). In addition, preliminary process modeling indicates that ALF meets the purity and recovery requirements set forth by the U.S. Department of Energy when operated in a simple heat-regenerated cycle. The performance, again, is favorable compared to that of other leading MOF systems (table S8 and figs. S31 to S33).

Last, another intriguing feature of ALF is that it could offer an efficient vehicle for long-term CO₂ storage in the future if the selective reduction of CO₂ to formic acid with solar hydrogen becomes more efficient (fig. S16) (24). CO₂ could then be stored in the stable ALF framework itself, according to the overall reaction $\text{Al}_2\text{O}_3 + 6\text{CO}_2 + 3\text{H}_2 \rightarrow 2\text{Al}(\text{HCOO})_3$. This reaction would yield a storage capacity for CO₂ of 81 weight % (not including additional CO₂ that could be stored in the channels). If ALF is filled completely with CO₂ and formic acid is sourced from captured CO₂, then ALF represents a CO₂ packing efficiency that is 96.35% of dry ice.

MATERIALS AND METHODS

Reflux synthesis and activation of Al(HCOO)₃

The as-made Al(HCOO)₃ was synthesized by modifying a reported procedure (14). In a typical synthesis, formic acid (100 ml) and aluminum hydroxide (1.2 g, 0.015 mol) were refluxed in a 250-ml three-neck round-bottom flask at 100°C (373 K) for 48 hours. After completing the reaction, excess formic acid was extracted by centrifugation, and the white solid was rinsed with a copious amount of ethanol and separated using vacuum filtration. The air-dried sample gave a yield of 95% white solid product of Al(HCOO)₃(CO₂)_{0.75}(H₂O)_{0.25}[HCOOH]_{0.25}/[guest included/as-made Al(HCOO)₃]. On the basis of our chemical analysis, it is likely that the actual as-made compound is Al(HCOO)₃(CO₂)_{0.75}(H₂O)_{0.50}, with two molecules in the LCs. Analytical CHN data for AlC_{3.75}H₄O₈ (molecular weight, 204 g/mol) are as follows: calculated weight percentages: C, 22.06%; H, 1.96%; and observed: C, 22.58%; H, 2.32%.

Hydrothermal synthesis of as-made Al(HCOO)₃ single crystals

In a typical synthesis, formic acid (7 ml) and aluminum hydroxide (50 mg, 0.234 mmol) were added into a Teflon liner and stirred at

room temperature for 30 min until they formed a homogeneous suspension. Then, the contents were placed in a 23-ml Teflon-lined Parr stainless steel autoclave and heated at 130°C (403 K) for 3 days followed by slow cooling to room temperature, giving colorless cubic crystals of aluminum formate [Al(HCOO)₃(CO₂)_{0.75}(H₂O)_{0.25}(HCOOH)_{0.25}]. The resulting crystals were washed with a copious amount of ethanol and separated using vacuum filtration. The air-dried sample gave a yield of 83% of as-made Al(HCOO)₃ single crystals.

Activation of as-made Al(HCOO)₃ to ALF

The air-dried, as-made Al(HCOO)₃(CO₂)_{0.75}(H₂O)_{0.25}(HCOOH)_{0.25} (0.5 g, 2.16 mmol) was heated at 150°C (423 K) for 24 hours under high vacuum (1×10^{-4} mmHg) or heated in air/ambient conditions at 180°C (453 K) for 24 hours, yielding quantitative amounts of the guest-free ALF. Analytical CHN data for AlC₃H₃O₆ (molecular weight, 162.03 g/mol) are as follows: calculated weight percentages: C, 22.24%; H, 1.87%; and observed: C, 21.23%; H, 1.93%.

Synthesis of MOF-74-Ni

MOF-74-Ni was synthesized on the basis of a literature method (25). In a 100-ml round-bottom flask equipped with a condenser, a suspension of dihydroxyterephthalic acid (1.03 g, 5.1 mmol) in deionized water (40 ml) was heated to reflux under strong magnetic stirring. In a separate flask, nickel acetate tetrahydrate (2.51 g, 10 mmol) was dissolved in deionized water (10 ml) at 80°C (353 K). The obtained light green nickel solution was added in one portion to the boiling ligand suspension under continuous stirring. The reaction mixture was further refluxed for 1 hour. The final suspension was filtered, and the yellow microcrystalline powder was washed with warm deionized water (50 × 3 ml) and methanol (20 × 2 ml) before being dried overnight at 80°C (353 K). The powder was degassed at 150°C (423 K) for 20 hours before the measurement of gas sorption isotherms.

Synthesis of UiO-66-(OH)₂

UiO-66-(OH)₂ was prepared according to the literature method (26, 27). Briefly, 2,5-dihydroxyterephthalic acid (1 g, ≈5 mmol) and ZrOCl₂·8H₂O (1.7 g, ≈5.2 mmol) were added in a 50 ml of water/acetic acid (20/30, v/v) mixture and heated under reflux (≈105°C, ≈378 K) for 1 day to afford a dark khaki powder. The powder was washed with deionized water three times before soaking in water and methanol each for 3 days at room temperature, during which the solvent was refreshed every day. After the final removal of methanol by decanting, the sample was activated under vacuum at 120°C (393 K) overnight for further modifications and characterizations.

Single-crystal x-ray diffraction of ALF

Single-crystal x-ray diffraction data were measured on ALF at 200°C (473 K) using a Bruker AXS D8 Venture Mo microfocus sources equipped with a Photon 100 complementary metal-oxide semiconductor active pixel sensor detector. The data collection and integration were carried out with APEX3 software. The structures were solved by direct methods, and refinement of the structure was performed by least squares procedures on weighted F^2 values using the SHELXL-2014 program package included in the WinGx system programs for Windows (28).

NPD of ALF and CO₂-dosed ALF

Neutron diffraction measurements were performed on a 1.23-g activated sample of ALF powder at the National Institute of Standards

and Technology Center for Neutron Research. Data were collected at the high-resolution neutron powder diffractometer, BT-1, using a Ge(311) monochromator with an in-pile 60' collimator, corresponding to a neutron wavelength of 2.079 Å. The sample was loaded into a vanadium sample can in a He environment glove box and sealed with a soldered lead O-ring onto a copper heating block containing a valved outlet for gas loading. After mounting the sample onto a bottom-loaded closed cycle refrigerator, the sample was reactivated at elevated temperatures under vacuum to remove possible residual helium. The sample was then cooled and measured at various temperatures for sufficient time to be able to perform high-quality Rietveld refinements or with 1-hour scans to obtain unit cell values on heating. For CO₂ dosing datasets, a custom calibrated gas dosing manifold setup with a known volume and an attached pressure gauge was used to either maintain static pressure or deliver specific stoichiometric equivalents.

NPD data were analyzed using the TOPAS 6 software suite (29). For consistency, Pawley refinement of the activated sample at 15 K was used to establish the peak shape used for all subsequent Pawley (30) and Rietveld refinements. Because of the high symmetry and quality of the neutron diffraction data, the CO₂ molecules did not require rigid body modeling. The CO₂ molecules were refined as atoms, instead of rigid bodies, with the thermal parameters of the LC CO₂ atoms fixed to the thermal parameter values of the SC CO₂ atoms.

Variable temperature x-ray diffraction

Variable temperature powder x-ray diffraction (PXRD) patterns were measured on a PanAnalytical X'pert PRO MRD x-ray diffractometer with Cu K α radiation ($\lambda = 1.5418$ Å, 30 kV, and 40 mA). PXRD patterns were recorded on pelletized (10 mm by 10 mm) as-made Al(HCOO)₃ at various temperatures between 25° and 280°C (298 to 553 K) with a heating rate of 5°/min, a step of 0.025°, and a scan speed of 1 s per step.

X-ray diffraction for stability analysis

PXRD patterns were measured on a Bruker D8 ADVANCED diffractometer with Cu K α radiation ($\lambda = 1.5418$ Å, 40 kV, and 40 mA). All the PXRD patterns were recorded from 10° to 60° (2 θ) with a step of 0.02° and a scan speed of 1 s per step under ambient conditions.

DFT procedures

DFT calculations were performed using the Vienna Ab initio Simulation Package code (31, 32) with the projected augmented wave potentials (33, 34), where the following electrons were treated explicitly: H, 1s¹; C, 2s²2p²; O, 2s²2p⁴; and Al, 3s²3p¹. The unknown exchange-correlation contribution was calculated using the GGA (19), and the van der Waals interactions were treated using the Grimme method (DFT + D3) (35). The wave functions were expanded with plane waves up to a kinetic energy cutoff of 520 eV. The first Brillouin zone was integrated over a 3 × 3 × 3 Monkhorst-Pack (36) *k*-point mesh. Structural relaxations were performed until the interatomic forces were less than 0.01 eV/Å. The adsorption energy of adsorbate M (M = CO₂, N₂, and H₂O) inside ALF was calculated as

$$E_{\text{adsorption}} = (E[\text{Al}(\text{HCOO})_3, n\text{M}] - E[\text{Al}(\text{HCOO})_3] - nE[\text{M}])/n$$

where *E*'s are the DFT total energies and *n* is the number of adsorbing molecules in the cubic unit cell. The total energy of the adsorbate

molecule was calculated by placing a single molecule at the center of a 15 × 15 × 15 Å³ box. The energy landscape of ALF was calculated by placing an adsorbate molecule at the center of the cavities (SCs and LCs), aligned along the [001] direction, and moved along a translation vector *t* = (*x*, *y*, *z*), where *x*, *y*, and *z* = −0.1, −0.05, 0.0, +0.05, and +0.1 in fractional units. Then, all oxygen atoms of CO₂ were relaxed using DFT, whereas other atoms and the unit cell were held fixed. For N₂ calculations, one of the nitrogen atoms in N₂ was kept fixed, whereas, for H₂O adsorption, oxygen atoms of H₂O were fixed.

For calculation of the mechanical properties, the same method as discussed above was used. Geometry optimization was performed on the basis of the primitive cell of the experimental crystal structure until the interatomic forces are less than 0.01 eV/Å. Then, the structure of Al(HCOO)₃ was reoptimized under following strains

$$\begin{pmatrix} 1 + \delta & 0 & 0 \\ 0 & 1 & \delta/2 \\ 0 & \delta/2 & 1 \end{pmatrix}$$

where $\delta = \pm 0.5\%$ and $\pm 1\%$. The elastic constants were extracted from stress-strain relationship using the method in a previous study (37).

Breakthrough measurements

The breakthrough experiments were conducted using a homebuilt setup shown in Fig. 4. The gas cylinders of Ar (99.95%), 15/85 CO₂/N₂ mixed gas, N₂ (99.95%), and He (99.95%) were purchased from Air Liquide Singapore Pte Ltd. The stainless-steel columns used for loading MOF powders are 4 cm long, and their internal column diameter is 0.3 cm. Metal mesh and cotton wool were placed at both ends of the column to prevent the system from being contaminated by sample powders/pellets. A glass fiber heating tape was used for controlling the setup temperature for column activation, regeneration, and breakthrough experiments at a temperature above room temperature. The temperature of the heating tape (Omega DHT-102040LD) was detected and controlled by an Omega thermocouple (5SC-TT-K-30-36) and a microcontroller (Omron E5CC), respectively. Gas composition at the exit of the column was determined by a mass spectrometer (Hiden QGA quantitative gas analysis system). The flow rate of each component gas was calculated by an internal Ar flow reference with a fixed flow rate of 5 ± 0.05 sccm (standard cubic centimeter per minute).

Before the breakthrough experiments, the adsorption columns were activated by purging a constant He flow (5 ± 0.1 sccm) through the column at predetermined temperatures [180°, 150°, and 120°C (453, 423, and 393 K) for ALF, MOF-74-Ni, and UiO-66-(OH)₂, respectively] for at least 12 hours until no solvent or moisture signal could be detected by the mass spectrometer. For dry gas breakthrough experiments, a 15/85 premixed CO₂/N₂ flow with a total flow rate of 2 ± 0.05 sccm was stabilized for 40 min before being introduced into the column. As for the experiments of wet gas breakthrough, a N₂ flow (2 ± 0.05 sccm) purging through the water reservoir [RH = 80.5% at 25°C (298 K) as determined by Omega RH318 hygro-thermometer] was used to saturate the adsorption columns before introducing the 15/85 CO₂/N₂ mixed gas (2 ± 0.05 sccm) into the column.

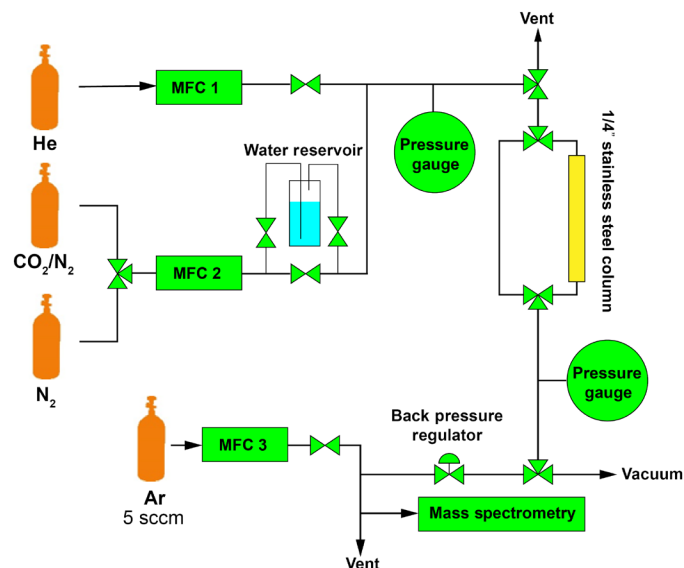


Fig. 4. A scheme of the breakthrough setup used in this study. MFC, Mass Flow Controller.

Adsorption capacity and selectivity calculations based on breakthrough data

On the basis of the mass balance of certain gas component in the mixed gas across the whole packed column (in – out = accumulation) including the dead volume of the setup (volume inside the setup excluding the column), it can be derived that

$$\varepsilon v_0 C_0 A t_c - \int_0^{t_c} \varepsilon v_t C_t A dt = LA\varepsilon C_e + LA(1 - \varepsilon)q_e + V_d C_e \quad (1)$$

where ε is the bed porosity estimated on the basis of the crystal density of the adsorbents, v_0 is the total interstitial gas velocity (meters per second) at the column inlet, C_0 is the inlet gas concentration (moles per cubic meter), A is the cross-sectional area of column (square meters), t_c is the elution time (seconds), v_t is the interstitial gas velocity (meters per second) at the exit of the column, C_t is the exit gas concentration (moles per cubic meter), C_e is the average gas concentration in the column (mole per cubic meter), V_d is the dead volume of the setup (cubic meters), L is the column length (meters), and q_e is the equilibrium concentration of adsorbate in the adsorbent (moles per cubic meter) corresponding to the average column pressure P_e (calculated *vide infra*).

By dividing both hand sides of Eq. 1 with the gas molar flow rate of this component at the column inlet, Eq. 1 will be rearranged as

$$\int_0^{t_c} \left(1 - \frac{F_t}{F_0}\right) dt = \frac{L}{v_0} \left(\frac{C_e}{C_0} + \frac{1 - \varepsilon}{\varepsilon} \frac{q_e}{C_0}\right) + \frac{V_d C_e}{F_0} \quad (2)$$

The gas concentration at the inlet of the column can be calculated by the following equation

$$C_0 = \frac{y_0 P_{in}}{R \times T} \quad (3)$$

where y_0 and P_{in} are the gas composition and pressure (kilopascals) at the inlet (upstream) of the column.

According to Darcy's law, we assume a linear pressure profile in the bed. Therefore, the average column pressure (P_e) and average gas concentration (C_e) can be calculated as

$$P_e \approx \frac{P_{in} + P_{out}}{2} \quad (4)$$

$$C_e \approx \frac{y_t P_e}{RT} = \frac{y_t (P_{in} + P_{out})}{2RT} \quad (5)$$

where y_t and P_{out} are the gas composition and pressure (kilopascals) at the outlet (downstream) of the column. Equation 2 can be further rearranged as

$$\int_0^{t_c} \left(1 - \frac{F_t}{F_0}\right) dt = \frac{L}{v_0} \left(\frac{P_{in} + P_{out}}{2P_{in}} + \frac{1 - \varepsilon}{\varepsilon} \frac{q_e}{C_0}\right) + \frac{V_d C_e}{F_0} \quad (6)$$

The dead volume item in the above equation can be obtained by performing the dead volume breakthrough experiments using the bypass of the setup and by performing the integration as

$$\int_0^{t_c'} \left(1 - \frac{F_t}{F_0}\right) dt = \bar{t}_{blank} = \frac{V_d C_e}{F_0} \quad (7)$$

where t_c' is the elution time of the dead volume breakthrough experiments and \bar{t}_{blank} is the mean residence corresponding to the setup dead volume.

Breakthrough selectivity was calculated using Eq. 8

$$S = \frac{q_{e1}/C_{e1}}{q_{e2}/C_{e2}} \quad (8)$$

where C_{ei} is the equilibrium concentration of component i in gas phase and q_{ei} is the gas concentration of component i in the adsorbent.

PBP correction of breakthrough curves of wet CO₂

Because the dead volumes of dry gas and wet gas breakthrough experiments are different, it is necessary to use the point-by-point (PBP) correction method (38) to calibrate the breakthrough curves before comparing the breakthrough time of CO₂ under dry and wet conditions. In this method, the corrected breakthrough time $t_{corrected}$ is calculated as

$$t_{corrected} = t - t_b \quad (9)$$

where t is the breakthrough time of a specific normalized flow rate F/F_0 in the breakthrough of adsorption column and t_b be the breakthrough time of the same normalized flow rate in the breakthrough experiment of a bypass column. Figure 5 visualizes the PBP correction of a breakthrough curve.

Gas adsorption experiments

Single-component gas sorption isotherms were measured on a Micromeritics 3-FLEX surface area and porosity analyzer instrument. For all the analysis, as-made Al(HCOO)₃ (100 mg) was heated at 150°C (423 K) for 24 hours using Smart VacPrep Micromeritics high vacuum degas instrument. After 24 hours, the sample tubes were transferred into the analysis chamber and continued further in situ activation at 150°C (423 K) for additional 6 hours using in situ preheating Micromeritics 3-FLEX vacuum chamber. The temperature on the analysis bath was precisely controlled using a Heidolph

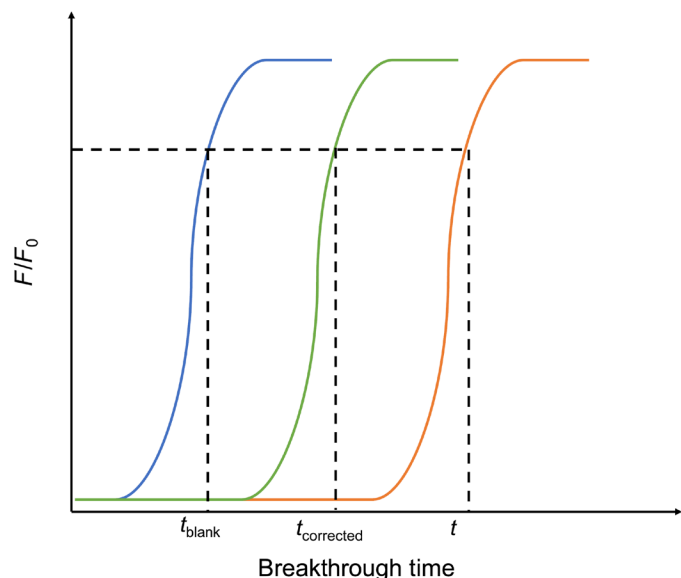


Fig. 5. A scheme showing the PBP correction of a breakthrough curve.

magnetic stirrer Hei-Tec hotplate with Pt 1000 temperature sensor control system. A saturated solution of dry ice and acetone mixture was used for collecting the 195-K isotherms, and liquid N₂ was used for collecting the 77-K N₂ isotherms.

Calculation of CO₂/N₂ sorption selectivity

The gas adsorption isotherms of CO₂ and N₂ were first fitted to the Langmuir (Eq. 10) and Henry model (Eq. 11), respectively

$$q = \frac{q_{\text{sat}} bp}{1 + bp} \quad (10)$$

$$q = K_H p \quad (11)$$

where q is the amount of adsorbed gas (millimoles per gram), p is the bulk gas phase pressure (kilopascals), q_{sat} is the saturation amount (millimoles per gram), b is the Langmuir-Freundlich parameter (per kilopascal), and K_H is the Henry constant (millimoles per gram per kilopascal).

Ideal adsorbed solution theory (IAST) starts from the Raoult's law type of relationship between fluid and adsorbed phase

$$P_i = Py_i = P_i^0 x_i \quad (12)$$

$$\sum_{i=1}^n x_i = \sum_{i=1}^n \frac{P_i}{P_i^0} = 1 \quad (13)$$

where P_i is partial pressure of component i (kilopascals), P is total pressure (kilopascals), and y_i and x_i represent mole fractions of component i in gas and adsorbed phase (dimensionless), respectively. P_i^0 is equilibrium vapor pressure (kilopascals).

In IAST, P_i^0 is defined by relating to spreading pressure π

$$\frac{\pi S}{RT} = \int_0^{P_i^0} \frac{q_i(P_i)}{P_i} dP_i = \Pi (\text{Constant}) \quad (14)$$

where π is spreading pressure, S is specific surface area of adsorbent (square meters per gram), R is gas constant (8.314 J K⁻¹ mol⁻¹), T is temperature (kelvin), and $q_i(P_i)$ is the single-component equilibrium obtained from isotherm (millimoles per gram).

For a Langmuir model, we have an analytical expression for the integral

$$\int_0^{P_i^0} \frac{q_i(P_i)}{P_i} dP_i = \Pi (\text{Constant}) = q_{\text{sat}} \ln(1 + b_A P_i^0) \quad (15)$$

For a Henry model, the analytical expression for the integral is

$$\int_0^{P_i^0} \frac{q_i(P_i)}{P_i} dP_i = \Pi (\text{Constant}) = K_H P_i^0 \quad (16)$$

The isotherm parameters will be known from the previous fitting. For a binary component system, the unknowns will be Π , P_1^0 , and P_2^0 , which can be obtained by simultaneously solving Eqs. 12 and 14 via the Python package pyLAST (39).

The adsorbed amount for each component in a mixture is

$$q_i^{\text{mix}} = x_i q_T \quad (17)$$

$$\frac{1}{q_T} = \sum_{i=1}^n \frac{x_i}{q_i(P_i^0)} \quad (18)$$

where q_i^{mix} is the adsorbed amount of component i (millimoles per gram) and q_T is the total adsorbed amount (millimoles per gram).

The adsorption selectivity S_{ads} can be calculated using Eq. 19.

$$S_{\text{IAST}} = \frac{q_1/q_2}{p_1/p_2} \quad (19)$$

Equilibrium-based process modeling for ALF and comparison with literature-reported sorbents

The essential principle behind adsorption separation is to exploit the difference in interactions of various components of the gas mixture with the porous media. A typical process will involve an adsorption phase where the feed gas is contacted with the porous media and CO₂ is preferentially sequestered, as well as a desorption phase at a different condition permitting the release of the trapped CO₂ from the sorbent. In general, regeneration is affected by decreasing the pressure (accordingly, pressure- or vacuum-swing adsorption) or increasing the temperature [accordingly, temperature-swing adsorption (TSA)].

The water affinity in ALF and a variety of other reported sorbents implies an uptake of water similar, if not exceeding, CO₂; hence, water is recovered alongside CO₂ as a heavy component. It is preferable to operate with part, if not all, of the cycle at an elevated temperature so as to circumvent the use of high vacuum ($P_L \ll 0.1$ bar) for the sorbent regeneration. Because the saturation pressure of water is ≈ 7 kPa at 313 K, it is impossible to extract water as a pure stream from the sorbent by applying vacuum higher than this level.

In light of the above consideration, we applied an equilibrium-based model of a TSA cycle with the purpose of estimating the process-level performance of ALF relative to other benchmark adsorbents. The model was described by Ajenifuja *et al.* (40) and covers a basic three-step process with adsorption, heating, and cooling steps (Fig. 6), with the following simplifying assumptions:

- 1) The bed is well mixed during the heating and cooling steps.
- 2) During the adsorption step, a discontinuous profile separating the initial concentration from the feed concentration propagates through the bed until breakthrough.
- 3) The pressure drop in the bed is negligible.
- 4) The adsorbed and gas phases are in thermal and chemical equilibrium.
- 5) Heat transfer resistances are negligible.
- 6) The specific heat capacity of the gas phase is negligible.
- 7) The gas phase is accurately described by the ideal gas law.

The CO₂ capture performance is analyzed on the basis of four performance indicators of the adsorbents, namely, product purity, product recovery, cyclic working capacity (WC), and specific thermal energy requirement.

The CO₂ purity is defined as

$$\text{Product purity} = \frac{N_{\text{CO}_2, \text{recovered}}}{N_{\text{CO}_2, \text{recovered}} + N_{\text{N}_2, \text{recovered}}} \quad (20)$$

where $N_{\text{CO}_2/\text{N}_2, \text{recovered}}$ is the molar amount of CO₂ or N₂ recovered in the heating step.

The recovery is defined as

$$\text{Recovery} = \frac{N_{\text{CO}_2, \text{recovered}}}{y_{\text{CO}_2, \text{feed}} N_{\text{feed}}} \quad (21)$$

where $y_{\text{CO}_2, \text{feed}}$ is the CO₂ composition in the feed and N_{feed} is the total molar amount of gases fed into the bed.

The cyclic WC is the molar amount of CO₂ recovered per unit mass of the adsorbent

$$\text{WC} = \frac{N_{\text{CO}_2, \text{recovered}}}{m} \quad (22)$$

The specific thermal energy requirement, sp_{thermal} , is the amount of heat required during the heating step per unit production of CO₂

$$sp_{\text{thermal}} = \frac{Q^{\text{heat}}}{N_{\text{CO}_2, \text{recovered}} \cdot Mw_{\text{CO}_2}} \quad (23)$$

where Q^{heat} is the total amount of energy input required by the heating step and Mw_{CO_2} is the molecular weight of CO₂.

Fourier transform infrared

Fourier transform infrared (FTIR) spectra were obtained using an Agilent Technologies Cary 600 series FTIR spectrometer operating

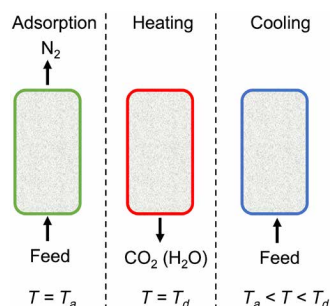


Fig. 6. A scheme of the three-step TSA cycle used in the shortcut model.

at ambient temperature. KBr was used as the window material for all the measurements. For the CO₂-reloaded experiments, CO₂ gas was passed into ALF (0.5 g) for 2 hours at ambient conditions. The FTIR spectra were measured by pressing ALF into a transparent thin pellet with KBr. For the water stability tests, 0.5 g of ALF was soaked in 7 ml of distilled water at room temperature for 12 hours. The vacuum-filtered air-dried ALF was directly subjected to FTIR analysis.

Thermogravimetric analysis

Thermogravimetric analysis (TGA) was carried out on the Q500 Thermogravimetric Analyzer. All the routine TGA analyses were done under a N₂ gas flow (60 ml/min + 40 ml/min, purge + protective). Both the samples [as-made Al(HCOO)₃ and ALF], ≈13 mg] were heated from room temperature to 400°C (673 K) with a heating rate of 10°/min.

TGA on 85/85 humid water treated ALFs

TGA was carried out on the Q500 Thermogravimetric Analyzer. All the TGA analyses were done under the N₂ gas flow (60 ml/min + 40 ml/min, purge + protective). Post-85/85 humid water-treated ALFs (≈15 mg) were heated from room temperature to 400°C (673 K) with a heating rate of 5°/min.

TGA CO₂ cycling

TGA cycling experiments were measured on the Q500 Thermogravimetric Analyzer. Cycling experiments were carried out under a CO₂ gas flow (60 ml/min) with protective N₂ gas (40 ml/min) for mass balance. For the analysis, freshly made ALF (12 mg) was loaded onto the aluminum pan and equilibrated at 40°C (313 K) for 120 min, heated up to 80°C (353 K) with a heating rate of 2°/min, and then cooled down to 40°C (313 K) with a cooling rate of 25°/min. The same experimental condition was repeated for 130 conjugative cycles without changing the sample amount and material from the TGA chamber.

For humid CO₂/N₂ experiments, TGA cycling tests between 40°C (313 K) and 80°C (353 K) were conducted for 50 cycles using 3% humid CO₂/N₂ (15/85). CO₂/N₂ (15/85) gas flow rate was 20.0 ml/min, and CO₂/N₂ (15/85) gas was exposed to the sample at 313 K for 30 min in each cycle before activation at 353 K.

Hydrolytic stability tests

Humidity studies were conducted on ALF samples made from as-made Al(HCOO)₃ (100 mg) samples that were activated for 24 hours at 180°C (453 K). Each ALF sample during the humidity stability studies was exposed to 85% humid water at 85°C (85/85) for time periods in between 1 and 24 hours in a Labec QHT-30 temperature and humidity chamber with a RH range of 25 to 98% and a temperature range of 20° to 120°C. After completion of respective exposure times (1 to 24 hours), each sample was then analyzed with PXRD, TGA, and CO₂ sorption tests.

CO₂ adsorption isotherms were measured following the hydrolytic treatment described above. Before the measurements, the samples (≈70 mg) were reactivated at 180°C (453 K) for 24 hours using Smart VacPrep Micromeritics high vacuum degas instrument. All the isotherms were measured at 50°C (323 K) on a Micromeritics 3-FLEX surface area and porosity analyzer instrument. After 24 hours, the sample tubes were transferred into the analysis chamber and underwent further in situ activation at 150°C (423 K) for an additional

6 hours using in situ preheating Micromeritics 3-FLEX vacuum chamber. The temperature on the analysis bath was precisely controlled using Heidolph magnetic stirrer Hei-Tec hotplate with Pt 1000 temperature sensor control system.

DVS experiments

Dynamic water vapor sorption measurements were performed on a gravimetric instrument (Hidden IGAsorp-CT, Warrington, UK) using CO₂ or N₂ as the carrier gas. The sample was first loaded at laboratory ambient conditions [21°C (294 K), 40% RH] and dried in situ by flowing dry nitrogen gas through the sample chamber at 120°C (393 K) for 6 hours. After drying, the temperature was lowered to 50°C (323 K). When CO₂ was used as the carrier gas, the inlet gas was switched at this point and the sample equilibrated for at least 2 hours until the mass was stable within 0.01 mg/min. Thereafter, the sample chamber was regulated to the measurement temperature (either 313, 323, or 333 K) and held for another 2 hours.

An adsorption-desorption cycle was performed by sequentially ramping the RH from 0 to 90/95% and back to 0% in fixed increments no more than 10% RH. RH is controlled by varying the proportion of dry and wet gas flowing into the sample chamber. For runs with CO₂ as carrier, direct measurement of RH is not possible due to sensor incompatibility, and hence, the RH is approximated by the relative proportion of wet gas, which is termed “wet concentration.” The mass change of the sample was recorded in real time and normalized against the initial (dry) weight. Cycles were repeated at least two times at each temperature, and the data for the second run are reported in fig. S36.

Because of mass loss of the samples throughout the measurements, only the run at 30°C (313 K) and CO₂ as carrier is reflective of multicomponent equilibria in ALF sorbent. The equilibrium uptake was estimated by instrument-accompanying analysis method, which regresses real-time kinetic data against an exponential uptake function. Isothermal uptake data for this run were reported as % mass change against wet concentration analogous to the DVS runs and are shown in fig. S37.

SUPPLEMENTARY MATERIALS

Supplementary material for this article is available at <https://science.org/doi/10.1126/sciadv.ade1473>

REFERENCES AND NOTES

- M. J. Lashaki, S. Khiavi, A. Sayari, Stability of amine-functionalized CO₂ adsorbents: A multifaceted puzzle. *Chem. Soc. Rev.* **48**, 3320–3405 (2019).
- M. Oschatz, M. Antonietti, A search for selectivity to enable CO₂ capture with porous adsorbents. *Energ. Environ. Sci.* **11**, 57–70 (2018).
- R. L. Siegelman, P. J. Milner, E. J. Kim, S. C. Weston, J. R. Long, Challenges and opportunities for adsorption-based CO₂ capture from natural gas combined cycle emissions. *Energ. Environ. Sci.* **12**, 2161–2173 (2019).
- M. Ding, R. W. Flaig, H.-L. Jiang, O. M. Yaghi, Carbon capture and conversion using metal-organic frameworks and MOF-based materials. *Chem. Soc. Rev.* **48**, 2783–2828 (2019).
- J. A. Mason, T. M. McDonald, T.-H. Bae, J. E. Bachman, K. Sumida, J. J. Dutton, S. S. Kaye, J. R. Long, Application of a high-throughput analyzer in evaluating solid adsorbents for post-combustion carbon capture via multicomponent adsorption of CO₂, N₂, and H₂O. *J. Am. Chem. Soc.* **137**, 4787–4803 (2015).
- J. M. Kollé, F. Mohammadreza, S. Abdelhamid, Understanding the effect of water on CO₂ adsorption. *Chem. Rev.* **121**, 7280–7345 (2021).
- P. Nugent, Y. Belmabkhout, S. D. Burd, A. J. Cairns, R. Luebke, K. Forrester, T. Pham, S. Ma, B. Space, L. Wojtas, M. Eddaoudi, M. J. Zaworotko, Porous materials with optimal adsorption thermodynamics and kinetics for CO₂ separation. *Nature* **495**, 80–84 (2013).
- W. Liang, P. M. Bhatt, A. Shkurenko, K. Adil, G. Mouchaham, H. Aggarwal, A. Mallick, A. Jamal, Y. Belmabkhout, M. Eddaoudi, A tailor-made interpenetrated MOF with exceptional carbon-capture performance from flue gas. *Chem* **5**, 950–963 (2019).
- S. Mukherjee, N. Sikdar, D. O’Nolan, D. M. Franz, V. Gascón, A. Kumar, N. Kumar, H. S. Scott, D. Madden, P. E. Kruger, B. Space, M. J. Zaworotko, Trace CO₂ capture by an ultramicroporous physisorbent with low water affinity. *Sci. Adv.* **5**, eaax9171 (2019).
- R. Vaidhyanathan, S. S. Iremonger, K. W. Dawson, G. K. Shimizu, An amine-functionalized metal organic framework for preferential CO₂ adsorption at low pressures. *Chem. Commun.* **35**, 5230–5232 (2009).
- T. T. T. Nguyen, J.-B. Lin, G. K. H. Shimizu, A. Rajendran, Separation of CO₂ and N₂ on a hydrophobic metal organic framework CALF-20. *Chem. Eng. J.* **442**, 136263 (2022).
- J.-B. Lin, T. T. T. Nguyen, R. Vaidhyanathan, J. Burner, J. M. Taylor, H. Durekova, F. Akhtar, R. K. M. Ghaffari-Nik, S. Marx, N. Fylstra, S. S. Iremonger, K. W. Dawson, P. Sarkar, P. Hovington, A. Rajendran, T. K. Woo, G. K. H. Shimizu, A scalable metal-organic framework as a durable physisorbent for carbon dioxide capture. *Science* **374**, 1464–1469 (2021).
- S. Deutz, A. Bardow, Life-cycle assessment of an industrial direct air capture process based on temperature–vacuum swing adsorption. *Nat. Energy* **6**, 203–213 (2021).
- Y.-Q. Tian, Y.-M. Zhao, H.-J. Xu, C.-Y. Chi, CO₂ template synthesis of metal formates with a ReO₃ set. *Inorg. Chem.* **46**, 1612–1616 (2007).
- H. A. Evans, Y. Wu, R. Seshadri, A. K. Cheetham, Perovskite-related ReO₃-type structures. *Nat. Rev. Mater.* **5**, 196–213 (2020).
- A. L. Spek, Single-crystal structure validation with the program PLATON. *J. Appl. Cryst.* **36**, 7–13 (2003).
- K. T. Leperi, R. Q. Snurr, F. You, Optimization of two-stage pressure/vacuum swing adsorption with variable dehydration level for postcombustion carbon capture. *Ind. Eng. Chem. Res.* **55**, 3338–3350 (2016).
- N. Nijem, H. Wu, P. Canepa, A. Marti, K. K. Balkus Jr., T. Thonhauser, J. Li, Y. J. Chabal, Tuning the gate opening pressure of metal-organic frameworks (MOFs) for the selective separation of hydrocarbons. *J. Am. Chem. Soc.* **134**, 15201–15204 (2012).
- J. P. Perdew, K. Burke, M. Ernzerhof, Generalized gradient approximation made simple. *Phys. Rev. Lett.* **77**, 3865–3868 (1996).
- S. Ehrlich, J. Moellmann, W. Reckien, T. Bredow, S. Grimme, System-dependent dispersion coefficients for the DFT-D3 treatment of adsorption processes on ionic surfaces. *Chem. Phys. Chem.* **12**, 3414–3420 (2011).
- A. F. Ismail, K. Khulbe, T. Matsuura, *Gas Separation Membranes: Polymeric and Inorganic* (Springer, 2015).
- M. M. F. Hasan, R. C. Baliban, J. A. Elia, C. A. Floudas, Modeling, simulation, and optimization of postcombustion CO₂ capture for variable feed concentration and flow rate. 2. Pressure swing adsorption and vacuum swing adsorption processes. *Ind. Eng. Chem. Res.* **51**, 15665–15682 (2012).
- J. C. Tan, A. K. Cheetham, Mechanical properties of hybrid inorganic-organic framework materials: Establishing fundamental structure–property relationships. *Chem. Soc. Rev.* **40**, 1059–1080 (2011).
- Chen, H. Xing, C. Wang, Z. Su, Highly efficient visible-light-driven CO₂ reduction to formate by a new anthracene-based zirconium MOF via dual catalytic routes. *J. Mater. Chem. A* **4**, 2657–2662 (2016).
- S. Cadot, L. Veyre, D. Luneau, D. Farrusseng, E. A. Quadrelli, A water-based and high space-time yield synthetic route to MOF Ni₂(dhtp) and its linker 2,5-dihydroxyterephthalic acid. *J. Mater. Chem.* **2**, 17757–17763 (2014).
- Z. Hu, Y. Wang, S. Farooq, D. Zhao, A highly stable metal-organic framework with optimum aperture size for CO₂ capture. *AIChE J.* **63**, 4103–4114 (2017).
- Y. Wang, Z. Hu, T. Kundu, Y. Cheng, J. Dong, Y. Qian, L. Zhai, D. Zhao, Metal-organic frameworks with reduced hydrophilicity for postcombustion CO₂ capture from wet flue gas. *ACS Sustain. Chem. Eng.* **6**, 11904–11912 (2018).
- G. M. Sheldrick, SHELXT—Integrated space-group and crystal-structure determination. *Acta Crystallogr.* **71**, 3–8 (2015).
- A. A. Coelho, TOPAS and TOPAS-Academic: An optimization program integrating computer algebra and crystallographic objects written in C++. *J. App. Cryst.* **51**, 210–218 (2018).
- G. S. Pawley, Unit-cell refinement from powder diffraction scans. *J. App. Cryst.* **14**, 357–361 (1981).
- G. Kresse, J. Furthmüller, Efficient iterative schemes for *ab initio* total-energy calculations using a plane-wave basis set. *Phys. Rev. B* **54**, 11169–11186 (1996).
- G. Kresse, J. Furthmüller, Efficiency of *ab-initio* total energy calculations for metals and semiconductors using a plane-wave basis set. *Comput. Mater. Sci.* **6**, 15–50 (1996).
- P. E. Blöchl, Projector augmented-wave method. *Phys. Rev. B* **50**, 17953–17979 (1994).
- G. Kresse, J. Hafner, Norm-conserving and ultrasoft pseudopotentials for first-row and transition elements. *J. Condens. Matter Phys.* **6**, 8245–8257 (1994).
- S. Grimme, J. Antony, S. Ehrlich, H. Krieg, A consistent and accurate *ab initio* parametrization of density functional dispersion correction (DFT-D) for the 94 elements H-Pu. *J. Chem. Phys.* **132**, 154104 (2010).
- J. D. Pack, H. J. Monkhorst, “Special points for Brillouin-zone integrations” – a reply. *Phys. Rev. B* **16**, 1748–1749 (1977).

37. Z. Deng, F. Wei, S. Sun, G. Kieslich, A. K. Cheetham, P. D. Bristowe, Exploring the properties of lead-free hybrid double perovskites using a combined computational-experimental approach. *J. Mater. Chem. A* **4**, 12025–12029 (2016).
38. A. Rajendran, V. Kariwala, S. Farooq, Correction procedures for extra-column effects in dynamic column breakthrough experiments. *Chem. Eng. Sci.* **63**, 2696–2706 (2008).
39. C. M. Simon, B. Smit, M. Haranczyk, pyIAST: Ideal adsorbed solution theory (IAST) Python package. *Comput. Phys. Commun.* **200**, 364–380 (2016).
40. A. Ajenifuja, L. Joss, M. Jobson, A new equilibrium shortcut temperature swing adsorption model for fast adsorbent screening. *Ind. Eng. Chem. Res.* **59**, 3485–3497 (2020).
41. A. Togo, I. Tanaka, First principles phonon calculations in materials science. *Scr. Mater.* **108**, 1–5 (2015).
42. K. Maninder, S. Farooq, Adsorbent screening for postcombustion CO₂ capture: A method relating equilibrium isotherm characteristics to an optimum vacuum swing adsorption process performance. *Ind. Eng. Chem. Res.* **55**, 2447–2460 (2016).
43. Compendium of carbon capture technology, U.S. Dept. of Energy (2020).
44. C. Chen, X. Feng, Q. Zhu, R. Dong, R. Yang, Y. Cheng, Microwave-assisted rapid synthesis of well-shaped MOF-74 (Ni) for CO₂ efficient capture. *Inorg. Chem.* **58**, 2717–2728 (2019).
45. S. Xiang, Y. He, Z. Zhang, H. Wu, W. Zhou, R. Krishna, B. Chen, Microporous metal-organic framework with potential for carbon dioxide capture at ambient conditions. *Nat. Commun.* **3**, 954 (2012).
46. D. Britt, H. Furukawa, B. Wang, T. G. Glover, O. M. Yaghi, Highly efficient separation of carbon dioxide by a metal-organic framework replete with open metal sites. *Proc. Natl. Acad. Sci. U.S.A.* **106**, 20637–20640 (2009).
47. A. Kumar, D. G. Madden, M. Lusi, K. J. Chen, E. A. Daniels, T. Curtin, J. J. Perry IV, M. J. Zaworotko, Direct air capture of CO₂ by physisorbent materials. *Angew. Chem. Int. Ed.* **54**, 14372–14377 (2015).
48. J. A. Mason, K. Sumida, Z. R. Herm, R. Krishna, J. R. Long, Evaluating metal-organic frameworks for post-combustion carbon dioxide capture via temperature swing adsorption. *Energ. Environ. Sci.* **4**, 3030–3040 (2011).
49. Z. Shi, Y. Tao, J. Wu, C. Zhang, H. He, L. Long, Y. Lee, T. Li, Y.-B. Zhang, Robust metal-triazolate frameworks for CO₂ capture from flue gas. *J. Am. Chem. Soc.* **142**, 2750–2754 (2020).
50. N. Nandi, S. Collins, D. Chakraborty, D. Banerjee, P. K. Thallapally, T. K. Woo, R. Vaidyanathan, Ultralow parasitic energy for postcombustion CO₂ capture realized in a nickel isonicotinate metal-organic framework with excellent moisture stability. *J. Am. Chem. Soc.* **139**, 1734–1737 (2017).
51. O. T. Qazvini, S. G. Telfer, MUF-16: A robust metal-organic framework for Pre- and post-combustion carbon dioxide capture. *ACS Appl. Mater.* **13**, 12141–12148 (2021).
52. A. Masala, J. G. Vitillo, F. Bonino, M. Manzoli, C. A. Grande, S. Bordiga, New insights into UTSA-16. *Phys. Chem. Chem. Phys.* **18**, 220–227 (2016).
53. C. A. Grande, R. Blom, V. Middelkoop, D. Matras, A. Vamvakeros, S. D. Jacques, A. M. Beale, M. Di Michiel, K. A. Andreassen, A. M. Bouzga, Multiscale investigation of adsorption properties of novel 3D printed UTSA-16 structures. *Chem. Eng. J.* **402**, 126166 (2020).
54. P. M. Bhatt, Y. Belmabkhout, A. Cadiau, K. Adil, O. Shekha, A. Shkurenko, L. J. Barbour, M. Eddaoudi, A fine-tuned fluorinated MOF addresses the needs for trace CO₂ removal and air capture using physisorption. *J. Am. Chem. Soc.* **138**, 9301–9307 (2016).
55. O. Shekha, Y. Belmabkhout, Z. Chen, V. Guillerm, A. Cairns, K. Adil, M. Eddaoudi, Made-to-order metal-organic frameworks for trace carbon dioxide removal and air capture. *Nat. Commun.* **5**, 4228 (2014).
56. K. J. Chen, D. G. Madden, T. Pham, K. A. Forrest, A. Kumar, Q. Y. Yang, W. Xue, B. Space, J. J. Perry IV, J. P. Zhang, X. M. Chen, Tuning pore size in square-lattice coordination networks for size-selective sieving of CO₂. *Angew. Chem. Int. Ed.* **128**, 10424–10428 (2016).
57. N. Huang, X. Chen, R. Krishna, D. Jiang, Two-dimensional covalent organic frameworks for carbon dioxide capture through channel-wall functionalization. *Angew. Chem. Int. Ed.* **127**, 3029–3033 (2015).
58. L. Stegbauer, M. W. Hahn, A. Jentys, G. Savasci, C. Ochsenfeld, J. A. Lercher, B. V. Lotsch, Tunable water and CO₂ sorption properties in isostructural azine-based covalent organic frameworks through polarity engineering. *Chem. Mater.* **27**, 7874–7881 (2015).
59. X. Guan, H. Li, Y. Ma, M. Xue, Q. Fang, Y. Yan, V. Valtchev, S. Qiu, Chemically stable polyarylether-based covalent organic frameworks. *Nat. Chem.* **11**, 587–594 (2019).
60. N. S. Wilkins, J. A. Sawada, A. Rajendran, Measurement of competitive CO₂ and H₂O adsorption on zeolite 13X for post-combustion CO₂ capture. *Adsorption* **26**, 765–779 (2020).
61. Y. Zhou, J. Zhang, L. Wang, X. Cui, X. Liu, S. S. Wong, H. An, N. Yan, J. Xie, C. Yu, P. Zhang, D. Yonghua, X. Shibo, L. Zheng, X. Cao, W. Yajing, Y. Wang, C. Wang, H. Wen, L. Chen, H. Xing, J. Wang, Self-assembled iron-containing mordenite monolith for carbon dioxide sieving. *Science* **373**, 315–320 (2021).
62. S. J. Datta, C. Khumnoon, Z. H. Lee, W. K. Moon, S. Doco, T. H. Nguyen, I. C. Hwang, D. Moon, P. Oleynikov, O. Terasaki, K. B. Yoon, CO₂ capture from humid flue gases and humid atmosphere using a microporous copper silicate. *Science* **350**, 302–306 (2015).
63. P. Q. Liao, X. W. Chen, S. Y. Liu, X. Y. Li, Y. T. Xu, M. Tang, Z. Rui, H. Ji, J. P. Zhang, X. M. Chen, Putting an ultrahigh concentration of amine groups into a metal-organic framework for CO₂ capture at low pressures. *Chem. Sci.* **7**, 6528–6533 (2016).
64. P. Q. Liao, H. Chen, D. D. Zhou, S. Y. Liu, C. T. He, Z. Rui, H. Ji, J. P. Zhang, X. M. Chen, Monodentate hydroxide as a super strong yet reversible active site for CO₂ capture from high-humidity flue gas. *Energ. Environ. Sci.* **8**, 1011–1016 (2015).
65. T. M. McDonald, J. A. Mason, X. Kong, E. D. Bloch, D. Gygi, A. Dani, V. Crocella, F. Giordanino, S. O. Odoh, W. S. Drisdell, B. Vlaisavljevich, Cooperative insertion of CO₂ in diamine-appended metal-organic frameworks. *Nature* **519**, 303–308 (2015).
66. T. M. McDonald, D. M. D'Alessandro, R. Krishna, J. R. Long, Enhanced carbon dioxide capture upon incorporation of N,N'-dimethylethylenediamine in the metal-organic framework CuBTTri. *Chem. Sci.* **2**, 2022–2028 (2011).
67. E. J. Kim, R. L. Siegelman, H. Z. Jiang, A. C. Forse, J. H. Lee, J. D. Martell, P. J. Milner, J. M. Falkowski, J. B. Neaton, J. A. Reimer, S. C. Weston, Cooperative carbon capture and steam regeneration with tetraamine-appended metal-organic frameworks. *Science* **369**, 392–396 (2020).
68. D. J. Fauth, M. L. Gray, H. W. Pennline, H. M. Krutka, S. Sjoström, A. M. Ault, Investigation of porous silica supported mixed-amine sorbents for post-combustion CO₂ capture. *Energ. Fuel* **26**, 2483–2496 (2012).
69. L. Jung-Hoon, R. L. Siegelman, L. Maserati, T. Rangel, B. A. Helms, J. R. Long, J. B. Neaton, Enhancement of CO₂ binding and mechanical properties upon diamine functionalization of M₂(dobpdc) metal-organic frameworks. *Chem. Sci.* **9**, 5197–5206 (2018).
70. D. F. Bahr, J. A. Reid, W. M. Mook, C. A. Bauer, R. Stumpf, A. J. Skulan, N. R. Moody, B. A. Simmons, M. M. Shindel, M. D. Allendorf, Mechanical properties of cubic zinc carboxylate IRMOF-1 metal-organic framework crystals. *Phys. Rev. B* **76**, 184106 (2007).
71. J.-C. Tan, B. Civalieri, C.-C. Lin, L. Valenzano, R. Galvelis, P.-F. Chen, T. D. Bennett, C. Mellot-Draznieks, C. M. Zicovich-Wilson, A. K. Cheetham, Exceptionally low shear modulus in a prototypical imidazole-based metal-organic framework. *Phys. Rev. Lett.* **108**, 095502 (2012).
72. H. Wu, T. Yildirim, W. Zhao, Exceptional mechanical stability of highly porous zirconium metal-organic framework UiO-66 and its important implications. *J. Phys. Chem. Lett.* **4**, 925–930 (2013).
73. A. U. Ortiz, A. Boutin, A. H. Fuchs, F.-X. Coudert, Anisotropic elastic properties of flexible metal-organic frameworks: How soft are soft porous crystals? *Phys. Rev. Lett.* **109**, 195502 (2012).

Acknowledgments: Certain commercial equipment, instruments, or materials are identified in this document. This identification does not imply recommendation or endorsement by the National Institute of Standards and Technology nor does it imply that the products identified are necessarily the best available for the purpose. Neutron diffraction data were collected at the NIST Center for Neutron Research (NCNR). The computational work was performed on resources of the National Supercomputing Centre, Singapore (www.nsc.sg). **Funding:** This work was supported by the National Research Council of the United States for financial support through the Research Associate Program (to H.A.E.), the NIST Center for Neutron Research (to H.A.E. and C.M.B.), the Singapore Ministry of Education Academic Fund Tier 1 (grants R-284-000-186-133 and R-284-000-194-114) (to P.C. and Z.D.), the Singapore MOE-Academic Research Fund (R-284-000-193-114) (to D.M., A.K.C., and J.W.), the National Research Foundation under the Fellowship NRF12-2020-0012 (to P.C.), the National University of Singapore Green Energy Programme for funding under the project code R-284-000-185-731 (to A.K.C., D.Z., J.W., and P.C.), the Ministry of Education—Singapore (MOE AcRF Tier 2 MOE 2018-T2-2-148 and MOE 2019-T2-1-093) (to Y.W., S.B.P., and D.Z.), and the Ras al Khaimah Centre for Advanced Materials (to A.K.C.). **Author contributions:** Conceptualization: A.K.C. Methodology: H.A.E., A.K.C., D.Z., and P.C. Investigation: H.A.E., D.M., Z.D., Y.W., P.C., D.Z., S.B.P., and F.W. Visualization: H.A.E. and Z.D. Funding acquisition: A.K.C., P.C., D.Z., and J.W. Supervision: A.K.C., P.C., D.Z., C.M.B., and J.W. Writing—original draft: H.A.E., A.K.C., D.M., Y.W., D.Z., P.C., and Z.D. Writing—review and editing: H.A.E., D.M., Y.W., Z.D., S.B.P., F.W., J.W., C.M.B., P.C., D.Z., and A.K.C. **Competing interests:** The authors declare the following competing financial interest: A patent has been filed by the National University of Singapore and Agency for Science Technology and Research based on the present results (SG nonprovisional application no. 10202106057Y). The authors declare that they have no other competing interests. **Data and materials availability:** All data needed to evaluate the conclusions in the paper are present in the paper and/or the Supplementary Materials. Experimental .cifs are deposited in the CCDC under numbers 2098658 - 2098663.

Submitted 27 July 2022
Accepted 12 September 2022
Published 2 November 2022
10.1126/sciadv.ade1473

Aluminum formate, Al(HCOO)₃: An earth-abundant, scalable, and highly selective material for CO₂ capture

Hayden A. EvansDinesh MullangiZeyu DengYuxiang WangShing Bo PehFengxia WeiJohn WangCraig M. BrownDan ZhaoPieremanuele CanepaAnthony K. Cheetham

Sci. Adv., 8 (44), eade1473. • DOI: 10.1126/sciadv.ade1473

View the article online

<https://www.science.org/doi/10.1126/sciadv.ade1473>

Permissions

<https://www.science.org/help/reprints-and-permissions>

Use of this article is subject to the [Terms of service](#)

Science Advances (ISSN) is published by the American Association for the Advancement of Science. 1200 New York Avenue NW, Washington, DC 20005. The title *Science Advances* is a registered trademark of AAAS. Copyright © 2022 The Authors, some rights reserved; exclusive licensee American Association for the Advancement of Science. No claim to original U.S. Government Works. Distributed under a Creative Commons Attribution NonCommercial License 4.0 (CC BY-NC).